Dynamic dose assessment by Large Eddy Simulation of the near-range atmospheric dispersion

Lieven Vervecken[1,2], Johan Camps[1] and Johan Meyers[2]

[1] SCK•CEN, Belgian Nuclear Research Centre, Boeretang 200, BE-2400 Mol, Belgium

[2] Department of Mechanical Engineering, KU Leuven, Celestijnenlaan 300, BE-3000 Leuven, Belgium

E-mail: lieven.vervecken@sckcen.be, johan.meyers@mech.kuleuven.be

Abstract. In order to improve the simulation of the near-range atmospheric dispersion of radionuclides, computational fluid dynamics (CFD) is becoming increasingly popular. In the current study, Large-Eddy Simulation (LES) is used to examine the time-evolution of the turbulent dispersion of radioactive gases in the atmospheric boundary layer, and it is coupled to a gamma dose rate model that is based on the point-kernel method with buildup factors. In this way, the variability of radiological dose rate from cloud shine due to instantaneous turbulent mixing processes can be evaluated. The steady release in an open field of ^{41}Ar and ^{133}Xe for 4 different release heights is studied, thus covering radionuclides that decay with a high-energy gamma and a low-energy gamma, respectively. Based on these simulations, the variability of dose rates at ground level for different averaging times in the dose measurements is analyzed. It is observed that turbulent variability in the wind field can lead to dose estimates that are underestimated by up to a factor of four when conventional long-term measurements are used to estimate the dose from short-term exposures.

This is an author-created, un-copyedited version of an article accepted for publication in Journal of Radiological Protection. IOP Publishing Ltd is not responsible for any errors or omissions in this version of the manuscript or any version derived from it. The Version of Record is available online at doi:10.1088/0952-4746/35/1/165 [Lieven Vervecken et al 2015 J. Radiol. Prot. **35** *165]*

1. Introduction

A proper estimation of the pollutant dispersion and the resulting dose received by the general public after a release of radionuclides in the atmosphere is indispensable to assess possible health risks during the nuclear emergency preparedness and response phases (IAEA, 2002). For the simulation of the near-range atmospheric dispersion, computational fluid dynamics (CFD) is becoming increasingly popular (see, e.g., de Sampaio et al., 2008; Punitha et al., 2008; Nakayama and Nagai, 2009). Either using Reynolds-Averaged Navier–Stokes (RANS) simulations or Large-Eddy Simulations (LES), CFD offers a large potential to increase the accuracy of the dispersion simulation with respect to existing models.

Vach and Duong (2011) performed a series of CFD simulations to quantify the ground concentration and deposition fields of passive particles presumably emitted from a nuclear power plant. The radioactive plume was represented as a collection of Lagrangian particles which were dispersed on a steady velocity background obtained using RANS turbulence modeling. A similar approach was followed by Gallego et al. (2010) in their effort to analyze the traveling distance of radioactive particles, emitted by a nuclear power plant. Despite the fact that no gamma dose assessment was performed in these studies, Raza and Avila (2001) illustrated that the resulting dose from these particles can be computed by treating each as a point source and by adding the contribution from each particle in the domain.

Instead of using the Lagrangian description, Xie et al. (2012) followed an Eulerian approach in combination with a RANS simulation of the wind field to simulate the dispersion of ^{222}Rn released from a uranium mine ventilation shaft. Subsequently, the effective dose rate to the public was estimated by multiplying the resulting concentration with dose conversion factors (Xie et al., 2014). Also Duarte et al. (2013) applied this approach for the radiological assessment of the fall of a radioactive waste package.

Instead of RANS, de Sampaio et al. (2008) used LES modeling and examined the time-evolution of the dispersion of radionuclides in the vicinity of nuclear power plants, illustrating the importance of the local phenomena on the dispersion problem. Also Fuka and Brechler (2012) and Nakayama et al. (2013) employed LES to simulate the dispersion of radioactive matter. The main advantages of LES over RANS are its improved accuracy, and the fact that dispersion due to turbulent eddies is better captured. Neither, however, coupled the LES model to a gamma dose rate model to assess the radiological dose from cloud shine. Such an analysis of a time-dependent simulation can provide keen insight into the behaviour of the gamma fluence rate at ground level. For the case presented in the current study, it is illustrated that the largest variability in local, instantaneous gamma dose rate is found at a distance of ten times the release height in stream-wise direction, regardless of the energy of the gammas. It is also demonstrated that the effective dose can be underestimated by up to a factor of four when long-term measurements are used to estimate the dose from short-term exposures and the variability in the wind field is neglected. This is of particular

interest when studying the optimization of measurement strategies, and when estimating measurement uncertainties related to atmospheric effects.

A time-dependent dose assessment model based on CFD for the simulation of the near-range dispersion of radioactive gases is presented. An Eulerian approach is used to simulate the pollutant dispersion where the concentration is formulated as a transient three-dimensional advection-diffusion problem. The instantaneous profiles for velocity and eddy viscosity are produced by a LES of the atmospheric boundary layer (ABL). The gamma dose rates are computed using the point-kernel method with buildup factors. Using this coupled model, a series of time-dependent simulations of a steady release of ^{41}Ar and ^{133}Xe for 4 different release heights into an open field are performed and the variability of the gamma dose rate from cloud shine at ground level is studied. Note that in some cases, in particular for a stable ABL, a release above the boundary layer is possible. This is not considered in the current study though the present method might be applied.

The paper is further organized as follows. First, in section 2, the pollutant dispersion model and the model used to perform the dose assessment are presented. Next, section 3 details the numerical setup of our simulations. The results of simulations are discussed in section 4. Finally, conclusions are presented in section 5.

2. Methodology

In this section, the large eddy simulation model used for the simulation of the pollutant dispersion is presented in §2.1. Next, the model employed in this work to perform the gamma dose assessment is briefly discussed in §2.2.

2.1. Pollutant dispersion model

In the current work, only the dispersion of radionuclides in the form of non-buoyant, non-reactive gases of in a thermally neutral atmospheric boundary layer is considered. By taking L as the pollutant release height, U as the mean wind speed at height L and R as the pollutant release rate, the non-dimensional time, distance, and concentration can be defined as $t^* = tU/L$, $x^* = x/L$, and $c^* = cUL^2/R$, respectively. An Eulerian approach is used to formulate the dispersion of the radionuclide as a transient three-dimensional advection-diffusion problem with radioactive decay. Neglecting the small effect of molecular diffusion, the evolution of the non-dimensional concentration is described by

$$\frac{\partial \tilde{c}^*}{\partial t^*} + \nabla^* \cdot (\tilde{\boldsymbol{u}}^* \, \tilde{c}^*) = \nabla^* \cdot \left(\tilde{\boldsymbol{u}}^* \tilde{c}^* - \widetilde{\boldsymbol{u}^* c^*} \right) - \lambda^* \tilde{c}^* + S^* \tag{1}$$

where the non-dimensional variables $\tilde{\boldsymbol{u}}^*(\boldsymbol{x}, t) = \tilde{\boldsymbol{u}}(\boldsymbol{x}, t)/U$ is the resolved velocity field (see below for its computation), $\tilde{\boldsymbol{u}}^* \tilde{c}^* - \widetilde{\boldsymbol{u}^* c^*}$ is the sub-grid scale pollutant flux, $\lambda^* = \lambda L/U$ is the radioactive decay constant, and where $S^* = SL^3/R$ is the pollutant

source. In order to model the sub-grid scale pollutant flux, an eddy-diffusivity approach is used, i.e. (Bird et al., 2006):

$$\tilde{\boldsymbol{u}}^*\tilde{c}^* - \widetilde{\boldsymbol{u}^*c^*} \approx \frac{\nu^*_{sgs}}{Sc_{sgs}}\nabla^*\tilde{c}^* \tag{2}$$

where Sc_{sgs} is the SGS Schmidt number, and $\nu^*_{sgs} = \nu_{sgs}/UL^2$ is the non-dimensional SGS eddy viscosity from (5) below. In the current study $Sc_{sgs} = 0.4$ is employed (adopted from Chamecki et al., 2009). Note that for small decay times or for very high wind speeds, λ^* is approximately zero and the pollutant concentration becomes independent from radioactive decay $\tilde{c}(\lambda^*, Sc_{sgs}) \approx \tilde{c}(0, Sc_{sgs})$.

The incompressible, filtered Navier–Stokes equations are solved in order to obtain the turbulent velocity field $\tilde{\boldsymbol{u}}^*(\boldsymbol{x}, t)$. The viscous term can be neglected because of the very high Reynolds number of the atmospheric flows and because the modeling of the wall layer (cf. section 3). In addition, also the Coriolis force can be neglected since the main focus of this work is in the lower layers of the ABL. Hence, the continuity and momentum equation read:

$$\nabla^* \cdot \tilde{\boldsymbol{u}}^* = 0 \tag{3}$$

$$\frac{\partial\tilde{\boldsymbol{u}}^*}{\partial t^*} + \tilde{\boldsymbol{u}}^* \cdot \nabla\tilde{\boldsymbol{u}}^* = \frac{1}{\rho^*}\left(-\nabla^*\tilde{p}^* - \nabla^* \cdot \boldsymbol{\tau}^*\right) \tag{4}$$

where $\tilde{p}^*$ is the non-dimensional pressure and $\boldsymbol{\tau}^*$ is the non-dimensional SGS stress tensor. The Smagorinsky model is applied to model the deviatoric part of this stress tensor, such that (using Einstein summation convention)

$$\tau^*_{ij} - \frac{1}{3}\delta_{ij}\tau^*_{kk} = -2\nu^*_{sgs}\tilde{S}^*_{ij} = -2(c_{s,\Delta}\Delta^*)^2|\tilde{S}^*_{ij}|\tilde{S}^*_{ij} \tag{5}$$

where $\tilde{\boldsymbol{S}}^* = [\nabla^*\tilde{\boldsymbol{u}}^* + (\nabla^*\tilde{\boldsymbol{u}}^*)^T]/2$ is the strain-rate tensor, $|\tilde{S}^*_{ij}| = (2\tilde{S}^*_{ij}\tilde{S}^*_{ij})^{1/2}$, and $\Delta^* = \Delta/L$ is the LES filter width. The trace of the SGS stress tensor, $\tau_{kk}/3$, is not explicitly modeled, but instead absorbed into the pressure as is common practice in LES of incompressible flow. The Lagrangian scale-dependent Smagorinsky model, as introduced in Bou-Zeid et al. (2005), is employed to obtain a space and time dependent estimation of $c_{s,\Delta}$.

2.2. Gamma dose assessment model

It is well established that the gamma fluence rate observed by a receptor located at $\boldsymbol{x_o} = (x_0, y_0, z_0)$ due to radioactive matter at location (x', y', z') can be computed using the point-kernel method with buildup factor (see, e.g., Slade, 1968). To obtain the non-dimensional fluence rate $\phi^* = \phi L^2/R$ at location $\boldsymbol{x_o}$ due to the whole plume, this approach is applied to the continuous concentration field by integrating over the full domain (see, e.g., Park et al., 2000):

$$\phi^*_{\boldsymbol{x_o}} = \frac{\lambda^*}{4\pi L}\int\int\int_V \frac{B(\mu, r)}{r^2}e^{-\mu r}c^*dx'dy'dz' \tag{6}$$

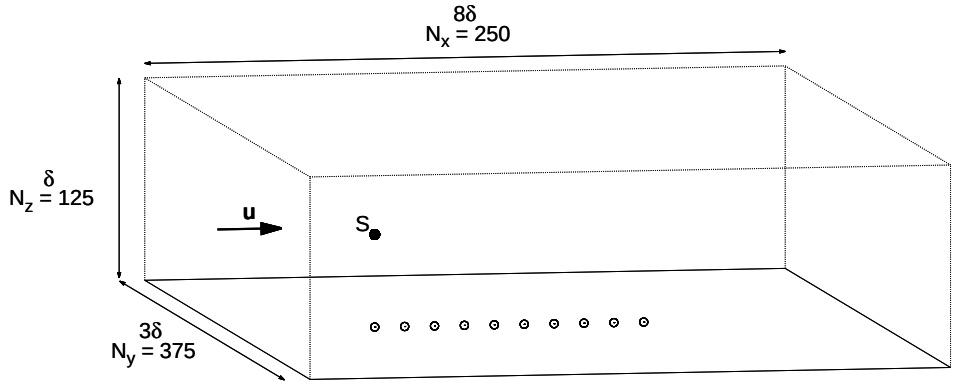

Figure 1: Outline of the simulated domain. Symbols: (•) Pollutant source; (○): monitoring point.

where $r^2 = (x_0 - x')^2 + (y_0 - y')^2 + (z_0 - z')^2$, V is the domain volume, μ is the linear attenuation coefficient in air and B is the dose buildup factor. Conversion of the local, non-dimensional fluence rate into the local dose rate can subsequently be achieved as

$$\dot{d}_{\boldsymbol{x}_\mathbf{o}} = \frac{K E_\gamma \mu_{en}}{\rho} \phi^*_{\boldsymbol{x}_\mathbf{o}} \frac{R}{L^2} \tag{7}$$

with $K = 1.6 \times 10^{-13}\,\mathrm{Gy\ kg\ MeV^{-1}}$ a unit conversion factor, E_γ the gamma energy released per disintegration, μ_{en} the energy absorption coefficient and ρ the density of the receptor. The buildup factor acts as a correction factor to include, e.g., secondary radiation due to Compton scattering in addition to the unscattered primary radiation (ANSI, 1991). Different expressions are found in the literature to evaluate the buildup factor (see, e.g., Chilton et al., 1984; Trubey, 1991). In this work, the parametrization in Taylor form is employed

$$B(\mu, r) = A\mathrm{e}^{-\alpha_1 \mu r} + (1 - A)\mathrm{e}^{-\alpha_2 \mu r} \tag{8}$$

where α_1, α_2 and A are tabled parameters, depending upon E_γ (ANSI, 1991). Sixth order polynomial fits in $\ln E_\gamma$ are constructed to compute α_1 and α_2, while linear interpolation is used to compute A.

3. Case set-up

First, the set of cases studied in this work is discussed in §3.1. The computational set-up used to solve the dispersion problem and to perform the dose assessment is elaborated in §3.2.

3.1. Case description

The geometry of the cases studied is very simple as shown in figure 1, i.e. an open field without any obstructions from buildings or vegetation. The simulation domain chosen is of size $8\delta \times 3\delta \times \delta$ where δ is the boundary layer thickness. The pollutant source is positioned $2/3\delta$ downstream from the inlet boundary, and in the middle of the domain

Table 1: Simulation characteristics.

Parameter	Value
Domain size	$8\delta \times 3\delta \times \delta$
Number of grid cells	$250 \times 375 \times 125 \sim 11.7$ million cells
Roughness length	$1.333 \times 10^{-5}\delta$ (short grassland)
Boundary layer thickness	750 m
Initial conditions	log-profile modified with random velocity fluctuations
Warm up period	stabilization of the total kinetic energy
Dose assessment frequency	every two time steps

in crosswind direction. Four different pollutant release heights are considered in this study, i.e. 0.06δ, 0.10δ, 0.14δ and 0.18δ, which correspond to 45 m, 75 m, 105 m and 135 m for a boundary layer with a thickness of 750 m. Fluence rates are monitored at ground level ($2 \times 10^{-3}\delta$ or 1.5 m for $\delta = 750$m) at multiple distances from the point of release along stream-wise direction as illustrated in figure 1.

Two noble gases are selected as the subject of our study i.e. ^{41}Ar and ^{133}Xe. These gases are inert and do not deposit. Both are frequently emitted in routine operation of various nuclear facilities (Rojas-Palma et al., 2004; Hu et al., 2010) and especially ^{133}Xe might be emitted in large quantities in nuclear accidents (Eslinger et al., 2014). A high energy gamma of $E_\gamma = 1\,293.64$ keV is emitted when ^{41}Ar decays to ^{41}K by beta minus decay with a decay constant of 105.36×10^{-6} s^{-1} (Bé et al., 2011). Conversely, a low energy gamma of $E_\gamma = 81.0$ keV is emitted during the beta minus decay of ^{133}Xe to ^{133}Cs. The decay constant of this process is 1.53×10^{-6} s^{-1} (Bé et al., 2008).

3.2. Computational set-up

The dose assessment problem is simulated using the OpenFOAM finite-volume open-source simulation platform. The main characteristics of the simulation are shown in table 1. The transport equations are discretized on a uniformly spaced, hexahedral mesh using second-order schemes. The second-order Crank–Nicholson scheme is applied for time discretization. Coupling between velocity and pressure is accomplished through the projection scheme (see, e.g. Önder and Meyers, 2014). A pressure gradient is imposed along the x-direction as the driving force of the flow. The pollutant source is modelled as a point source by simply adding a source term to the corresponding cell in the domain.

Periodic boundary conditions are set in the horizontal directions for all variables, therefore simulating a domain of infinite depth and width. For the concentration, Neumann boundary conditions are applied at the other boundaries. To suppress recycling of the pollutant to the inlet, an additional sink term $-\alpha C$ is added to the concentration equation with $\alpha = 0.5$ for $7\delta < x < 8\delta$ and $\alpha = 0$ otherwise. For the velocity, a stress boundary condition is imposed at the bottom of the domain to simulate

the effect of the wall layer (see, e.g., Bou-Zeid et al., 2005):

$$\tau_{i,3}^{wall}(x,y) = -\left[\frac{\kappa}{\ln(dz/2z_0)}\right]^2 (\hat{\tilde{u}}_1^2 + \hat{\tilde{u}}_2^2)^{1/2} \left[\hat{\tilde{u}}_i(x,y,dz/2)\right] \tag{9}$$

where $\kappa = 0.4$ is the von Kármán constant, dz is the height of the first grid cell, z_0 is the roughness length, u_1 and u_2 are the horizontal velocity components (index 3 indicates the vertical component), a tilde and a caret represent a quantity filtered at grid scale (Δ) and at test-filter scale (2Δ), respectively. In addition, the vertical velocity is set to zero. At the top of the domain, a symmetry condition is imposed.

The gamma fluence rate integral (6) is simply evaluated as the sum of the contribution of each cell individually:

$$\phi^*_{\boldsymbol{x_o}} = \frac{\lambda^*}{4\pi L} \sum_i \frac{B(\mu, r_i)}{r_i^2} \mathrm{e}^{-\mu r_i} V_i c_i^* \tag{10}$$

where r_i is now the distance from $\boldsymbol{x_o}$ to the cell-centre of cell i and V_i is the volume of cell i. Hence, each cell in the domain is treated as a radioactive point source. However, this approach becomes inaccurate for grid points close to the source. Therefore, the cells with a centre within a radius $V_r^{1/3}$ from the receptor are not included in (10), where V_r refers to the volume of the cell in which the receptor is located. Instead, the average concentration over these cells is computed and this is used to integrate (6) analytically over a spherical volume equal to the total volume of all cells included in the average. Note that this filtering operation is an approximation (for a discussion, see Kenis et al., 2013). Since the small time step required for stability of the dispersion simulation is not crucial for an accurate dose assessment, the integration is only performed every two time steps.

The simulations were carried out on 48 processors distributed over four nodes, installed with dual hexa-core Intel Xeon X5650 processors and interconnected through DDR infiniband. On this system, the warm up period to develop the flow field takes 13 days. Afterwards, the flow field simulation, the dispersion simulation and the dose assessment run simultaneously at a rate of 125 seconds real time per simulated second. Because post-processing is performed on the fly, the required storage space is limited to 1.9 Gb. Finally, the discussion is limited to fluence rates rather than dose rates to eliminate the effect of the receptor characteristics on the result. But recall that a conversion can be readily achieved using (7).

4. Results and discussion

The results of the cases studied are presented in this section. First, in §4.1, the results of a typical simulation are presented i.e. the dispersion of ^{41}Ar from 0.1δ altitude. Subsequently, a comparison is made between the full set of simulations in §4.2. Finally, in §4.3, the relevance of time-dependent fluence rate analyses for accident scenarios are discussed.

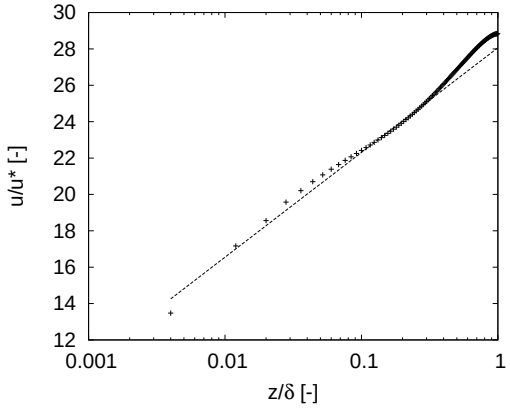

Figure 2: Planar and time-averaged vertical velocity profile $\langle u_1 \rangle / u_\tau$ (+) and theoretical profile $\langle u \rangle / u_\tau = (1/\kappa) \ln(z/z_0)$ with $\kappa = 0.4$ and $z_0 = 1.333 \times 10^{-5}\delta$ (- - - -).

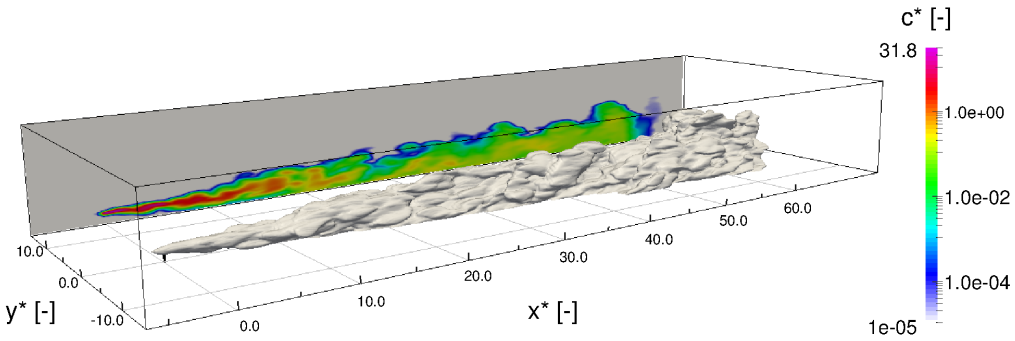

Figure 3: Instantaneous ^{41}Ar concentration c^* ($= cUL^2/R$), released from 0.1δ altitude. In gray, isosurface for $c^* = 10^{-5}$; Back plane, concentration in the stream-wise, vertical cross section through the point of release.

4.1. Typical simulation result: ^{41}Ar dispersion from 0.1δ altitude

The dispersion of ^{41}Ar from 0.1δ altitude is selected as a typical example to discuss the simulation results. In figure 2, the plane- and time-averaged vertical profile of the stream-wise velocity component (u_1) is shown. It is observed that this profile follows the theoretical logarithmic profile of the log-layer fairly well in the lower part of the domain. Further up ($z/\delta > 0.2$), the profile departs from the logarithmic distribution as expected (see, e.g., Bou-Zeid et al., 2005). It is found that increasing the vertical grid resolution reduces the small discrepancy between the actual and the theoretical profile in the lower part of the log-layer. The sudden drop in velocity at the cell closest to the wall, however, also results from the discretization but is independent of the grid resolution and can therefore not readily be corrected for (Wu and Meyers, 2013). Because the velocity profile behaviour is consistent with other sources, it is argued that the boundary layer flow is captured satisfactory by the present model.

An instantaneous, three-dimensional isosurface of the concentration $c^* = 10^{-5}$ is

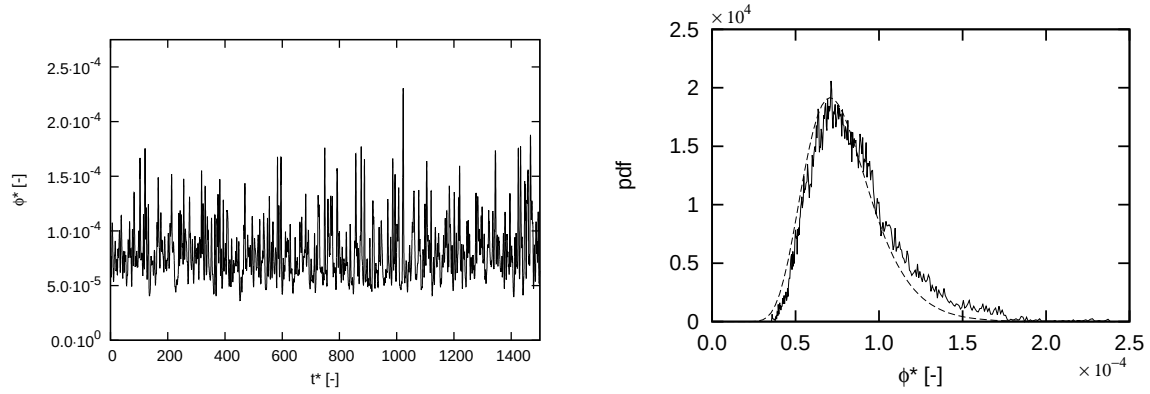

(a) (b)

Figure 4: Observed non-dimensional gamma fluence rate ϕ^* ($= \phi L^2/R$) at $x^* = 10$ ($= x/L$) due to the emission of ^{41}Ar from 0.1δ altitude. (a) Instantaneous observations, (b) Corresponding pdf (——) with best-fit log-normal distribution (- - - -).

shown in figure 3. The turbulent nature of the boundary layer clearly results in a non-uniform plume with a spread increasing with the distance from the point of release. When looking at the concentration in the vertical cross section through the point of release, plotted on the back plane of figure 3 (the plane is offset for the sake of visualization), the largest concentration is found in the direct proximity of the pollutant source and strongly decreases with downwind distance. Halfway along the domain, the peak concentration has dropped two orders of magnitude with respect to the maximum concentration, found close to the pollutant source. Correspondingly, the more uniform colouring at larger distance from the pollutant source implies smaller concentration gradients compared to close to the source.

In figure 4a, a part of the simulated time evolution of the non-dimensional gamma fluence rate ϕ^* is shown, observed at distance $x^* = 10$ downwind from the pollutant source, as a function of the non-dimensional time t^*. It is observed that the fluence rate is very noisy, showing a large number of peaks and troughs. The peaks, however, are significantly larger in magnitude with respect to the mean than the troughs. This is explained as follows. Because of the inverse proportionality with the square of the distance, concentration fluctuations in the vicinity of the observation point affect the fluence rate the strongest. A peak occurs when the plume immerses the observation point and, conversely, a trough occurs when the pollutant concentration in the vicinity of the observation point is low. Nevertheless, despite the fact that the concentration field is time-dependent, the total amount of pollutant in the proximity of an observation point is relatively constant in time due to the constant release rate. Thus, since the fluence rate is influenced by the whole domain (cf. (6)), a minimal fluence rate is always present. This minimum rate limits the depth of the troughs.

Looking at the corresponding probability density function (pdf) in figure 4b, it is observed that the data is positively skewed with a mode equal to a fluence rate of

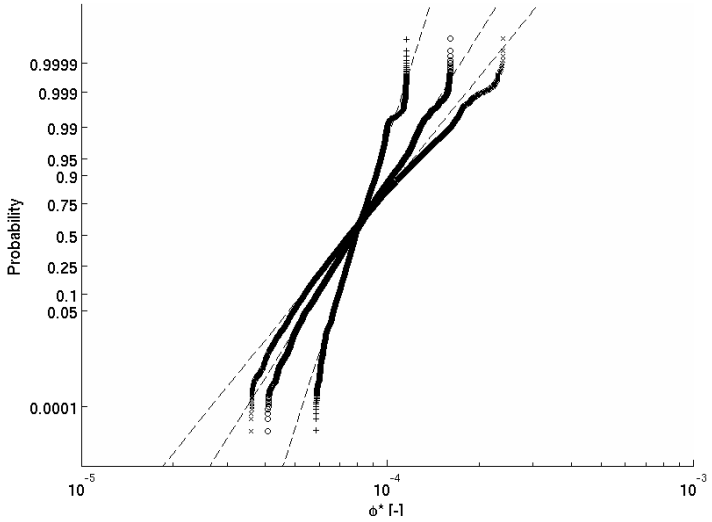

Figure 5: Probability plot of the observed non-dimensional gamma fluence rate ϕ^* ($= \phi L^2/R$) at $x^* = 10$ ($= x/L$) due to the emission of ^{41}Ar from 0.1δ altitude, instantaneous ($\times$), time-averaged with $\Delta t^* = 25$ ($\circ$) and time-averaged with $\Delta t^* = 125$ ($+$).

7.2×10^{-5} and a mean equal to 8.0×10^{-5}. For the sake of comparison, the pdf of the best-fit log-normal distribution $\ln \mathcal{N}(0.265, 0.284)$ is also added to this graph. Note that other presumed pdfs such as, e.g. the beta distribution, might also be relevant to use. While the left tails are very similar, the right tail of the true pdf is significantly heavier compared to the log-normal distribution.

By computing a moving average of the instantaneous fluence rate, the effect of deriving the gamma fluence rate from time-integrated measurement is examined. To this end, $\Delta t^* = 25$ and $\Delta t^* = 125$ are chosen as averaging times. This corresponds, e.g., to 5 and 25 minutes, respectively, for a boundary layer with $\delta = 750$ m and $U = 22.5$ km/h at a height of 75 m. A probability plot of the instantaneous and the time-averaged observations is shown in figure 5. The axes of this graph are chosen such that a log-normal distribution results in a straight line. For the sake of reference, the best-fit log-normal distributions for each of the observations are also shown in this graph. It is observed that near the mean value, the probability curves of the observations and the log-normal distribution match closely. But unlike the log-normal distribution, the ranges in fluence rates are clearly finite with distinct minima and maxima. It is readily understood that increasing the averaging time, reduces the spread on the observations by increasing the minimum and decreasing the maximum. Regardless of the averaging time, steeper slopes of the curves and lower probabilities are found at lower fluence rates. This points to lighter left tails compared to the log-normal distribution, while the more moderate slopes and lower probability at higher fluence rates imply heavier right tails.

In figure 6, the time-averaged non-dimensional gamma fluence rate is shown as a function of the distance from the point of release along the stream-wise direction.

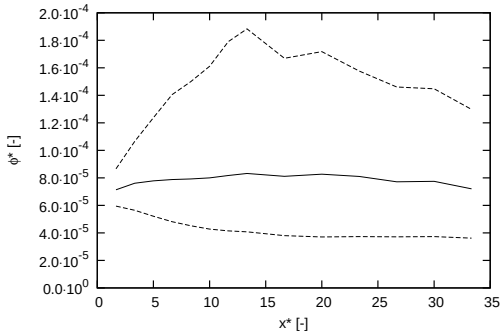

Figure 6: Time-averaged non-dimensional gamma fluence rate ϕ^* ($= \phi L^2/R$) at ground level due to ^{41}Ar emission from 0.1δ altitude (——) and 1$^{\text{st}}$–99$^{\text{th}}$ percentiles (- - - -) along the stream-wise direction.

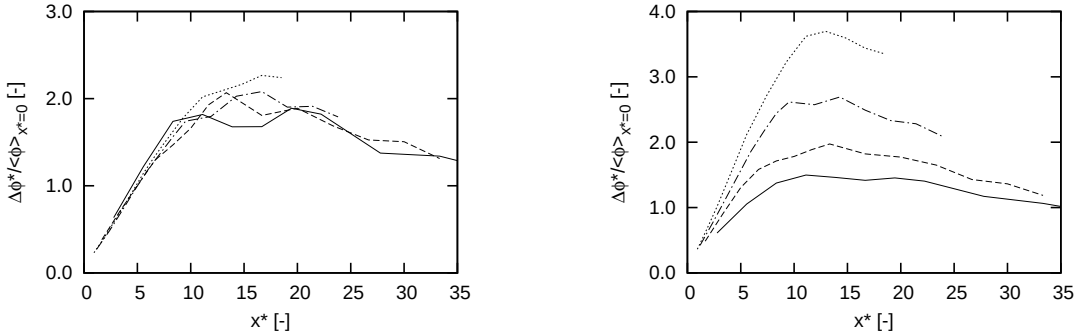

(a) (b)

Figure 7: Interval width between the 1$^{\text{st}}$ and 99$^{\text{th}}$ gamma fluence rate percentiles as a function of the non-dimensional distance x^*, scaled by the time-averaged non-dimensional gamma fluence at $x^* = 0$ for the release of ^{41}Ar (a), and ^{133}Xe (b). Lines: pollutant release height of 0.06δ (——); 0.10δ (- - - -); 0.14δ (— · —); 0.18δ (· · · · · ·).

The time-averaged fluence rate is fairly constant along the stream-wise direction for the range plotted with a value between 7.0×10^{-5} and 8.3×10^{-5}. In order to illustrate the spread on the instantaneous observations, the 1$^{\text{st}}$ and 99$^{\text{th}}$ percentiles are also shown in figure 6. The 1$^{\text{st}}$ percentile is found to decrease monotonically although the rate of decrease diminishes significantly after $x^* = 10$. The 99$^{\text{th}}$ percentile initially increases strongly with increasing distance and peaks at $x^* \approx 13$. Downstream of this point, a steady decrease is observed.

4.2. Comparison of the full set of simulations

The fluence rate due to the release of two noble gases released in an open field from four different altitudes is studied in this work. Hence, in total eight simulations are performed.

In order to compare the variability in gamma fluence rate observed in these simulations, the evolution of the interval widths between the 1$^{\text{st}}$ and 99$^{\text{th}}$ gamma fluence

rate percentiles as a function of x^* are considered. These are shown in figure 7 for the emission of ^{41}Ar (a) and ^{133}Xe (b). For the sake of comparison, the interval widths are rescaled by the time-averaged non-dimensional gamma fluence observed at $x^* = 0$. Right below the point of emission, the interval width equals approximately 20% of the mean fluence rate observed at $x^* = 0$ for all of the cases. It is found that in all cases the width first increases, reaching a maximum at $x^* \approx 13 \ldots 17$, and decreases afterwards but at a lower rate. This may indicate that the location of the maximum spread on the measurements is invariable when expressed in terms of the emission height.

The occurrence of the maximum of the interval width is related to two competing effects. On the one hand, concentration gradients falling within the sphere of influence of the receptor, result in a variation of the fluence rate. With increasing downstream distance, a larger part of the plume falls within this sphere of influence, due to the increase in plume spread. Thus, more variation in fluence rate is observed. On the other hand, the pollutant diffusion weakens the concentration gradients with increasing downstream distance. As the plume becomes better mixed, the variation in fluence rate decreases. The competition between the increase and decrease in the variation in fluence rate with increasing downstream distance due to the first and the second effect, respectively, results in the peak observed.

In case of the high energy gamma emitted by ^{41}Ar, the maximum width is approximately twice the mean fluence rate observed at $x^* = 0$, regardless of the emission height. For low-energy gammas however, there is a clear dependence on release height as illustrated in figure 7b. For the ^{133}Xe emission from 0.06δ altitude, the maximum is approximately 1.3 while this increases up to 3.8 for the emission from 0.18δ altitude. This difference is directly attributable to the energy dependence of the linear attenuation coefficient and the buildup factor. Since high energy gammas undergo less attenuation in air compared to low energy gammas, the spatial dependence becomes more important for the latter. This effect is amplified by the energy dependence of the buildup factor.

Finally, a practical illustration of the model applied to the dispersion of ^{41}Ar and ^{133}Xe can be found in table 2. For a boundary layer with $\delta = 750$ m and $U = 22.5$ km/h at a height of 75 m, the table shows the mean fluence rate at 375 m, 750 m, 1 500 m and 2 250 m downstream from the source, measured at 1.5 m above ground level. The 1^{st}-to-99^{th}-percentile interval width are also added to the table, expressed as a fraction of the mean fluence rate, for an averaging time of 30 seconds, and 1, 2, 5, 10 and 25 minutes, respectively. The pollutant is released from 75 m altitude at a rate of 1 MBq/s and the surface roughness is set to 0.01 m.

The maximum mean fluence rate is for both isotopes found between 750 m and 1 500 m from the point of release, though all values are very close together. It is observed that for an averaging time of 30 seconds, the spread of the measurements remains very large with values of the same order of magnitude as the mean fluence rate. By increasing the averaging time to 25 minutes, the spread is reduced by a factor 7. For instance at 375 m, the resulting spread for 25 minute averages is 11% and 17% of the mean fluence rate for ^{41}Ar and ^{133}Xe, compared to 78% and 102% for 30 second averages.

Table 2: Practical example of a pollutant release from a height of 75 m at a rate of 1 MBq/s for a boundary layer with $\delta = 750$ m and $U = 22.5$ km/h at release height.

	Distance from source [m]	Mean fluence rate [1/m^{2}s]	1^{st}-to-99^{th}-percentile interval width [% of mean fluence rate]					
			30 sec	1 min	2 min	5 min	10 min	25 min
^{41}Ar	375	468	78	64	46	30	20	11
	750	482	129	99	73	47	36	21
	1500	498	153	133	104	68	54	31
	2250	466	132	119	98	70	53	34
^{133}Xe	375	1432	102	80	56	35	25	17
	750	1462	146	121	90	57	38	26
	1500	1412	159	139	109	68	49	32
	2250	1276	137	127	102	70	50	35

4.3. Discussion

The variability of time-averaged fluence rates when averaged over different time windows has relevance for accident scenarios. In case of an accident, e.g. during which an individual located outside is to take shelter, the dose received by the individual is the critical parameter. Thus, the local dose rate has to be integrated over time and along the trajectory of the individual. The fence monitoring systems in nuclear installations usually output time-integrated dose rate data every 10 to 20 minutes. These measurements are a good indication of the average dose rate during an emission, i.e. the typical spread on the mean remains within 10 (cf. table 2 and discussion above). Thus, these measurements are, e.g., useful for estimating the source term of an unknown release. When considering the exposure of an individual during an accident however, the exposure time might be significantly shorter than the output time of the monitoring systems. It is therefore important to take the time scales of exposure, and the dominant turbulent time scales into account. The latter are primarily responsible for the variability of the fluence rate, meaning that the fluence rate is approximately constant over these periods of time. A full analysis of a detailed scenario is beyond the scope of the current paper, but in the following, a simple order of magnitude estimation is presented to demonstrate that 10 minute average dose rates may be inaccurate for dose assessments during evacuation scenarios.

Consider an individual, located within the exclusion area, normally demarcated by a fence at distance of 300 m to 800 m around the nuclear installation (Graham, 2012), who must take shelter inside a building. Presuming a distance of 100 m to the nearest building, it takes the average individual about 40 s to take shelter. This is significantly shorter than the characteristic time scale of large turbulent structures in the atmospheric

boundary layer. These consist of long streak-like structures with a typical length of 2 to 4 km. With a convection velocity of 10 m/s this leads to time scales in the order of 3 to 6 minutes. Since the mean variation of the plume is driven by this time scale, the instantaneous dose rate during the 40 s exposure will be nearly constant and therefore close to the average dose rate. Thus, the dose received by the individual during the exposure can deviate up to a factor of four from the mean dose, measured by the fence monitoring systems (cf. figure 7b). In general, this is true when the time required to cover the distance is short relative to the turbulent time scales. Consequently, fence monitoring data should be handled with caution when it is used to estimate the resulting dose from a short-term exposure.

5. Conclusion

In the current study, a time-dependent dispersion model for the near-range dispersion of radioactive gases in a thermally neutral atmospheric boundary layer is presented. To this end, a CFD model using LES turbulence modeling is coupled with a gamma dose rate model based on the point-kernel method with buildup factors. The variability of the gamma fluence rate at ground level was assessed by performing a set of time-dependent simulations of a constant release of a radioactive gas into an open field. Four different release heights were considered in this study as well as two different isotopes, i.e. ^{41}Ar emitting a high energy gamma and ^{133}Xe emitting a low energy gamma.

The simulations demonstrated that even with the very simple setup of the open field, a strongly fluctuating gamma fluence rate with a clear lower and upper bound was observed at ground level. At a distance of approximately fifteen times the release height, this variability was found to be maximal, regardless of the release height or the gamma energy. Note that this observation is only valid for the current simple release geometry and neutral atmospheric stratification. For high energy gammas of ^{41}Ar, the spread on the observations is not affected by the release height while this is the case for low energy gammas of ^{133}Xe. For both cases, this spread can be reduced effectively by performing time-averaging. However, it is illustrated neglecting this variability can result in errors up to a factor of four on the dose estimation when long-term measurements are used to estimate the resulting dose from short-term exposures. This information can be particularly useful in uncertainty quantification studies and for the optimization of measurement strategies.

The current work was limited to an open-field case, where effects of buildings or vegetation do not play a dominant role. In case of more complex geometries, locally generated turbulence can play an important role, and sometimes dominate the dispersion process. Also the thermal stratification of the ABL can have a non-negligible impact on the variability of the dose rate. Stable stratification suppresses turbulence and, as a result, the variability of the dose rate is expected to decrease. The opposite is true for a convective boundary layer. These are interesting topics for further research.

Acknowledgments

All simulations were carried out using the computing infrastructure of the Flemish Supercomputer Centre (VSC), funded by the Hercules Foundation and the Flemish Government. We thank Kevin Kenis for his contribution to the implementation of the fluence rate model.

References

ANSI 1991 *American National Standard for Gamma-ray Attenuation Coefficients and Buildup Factors for Engineering Materials* ANSI/ANS-6.4.3-1991 (The Society) p 119

Bé M M, et al. (2008) Table of Radionuclides (vol. 4A= 133 to 252). (Sèvres: Bureau International des Poids et Mesures) p 282

Bé M M, et al. (2011) Table of Radionuclides (vol. 6A= 22 to 242). (Sèvres: Bureau International des Poids et Mesures) p 278

Bird R, Stewart W and Lightfoot E 2006 *Transport Phenomena* vol 2 (New York: Wiley) p 905

Bou-Zeid E, Meneveau C and Parlange M B 2005 A scale-dependent Lagrangian dynamic model for large eddy simulation of complex turbulent flows *Physics of fluids* **17**:2 025105

Chamecki M, Meneveau C and Parlange M B 2009 Large eddy simulation of pollen transport in the atmospheric boundary layer *Aerosol Science* **40** 241–55

Chilton A B, Shultis J K and Faw R E 1984 *Principles of Radiation Shielding* (New Jersey: Prentice-Hall) p 488

Duarte J P, Frutuoso e Mel P, Alves A and Passos E 2013 Atmospheric Dispersion and dose Evaluation Due to the Fall of a Radioactive Package at a LILW Facility *International Journal of Energy Engineering* **3** 119–26

de Sampaio P, Junior M and Lapa C 2008 A CFD approach to the atmospheric dispersion of radionuclides in the vicinity of NPPs *Nuclear Engineering and Design* **238** 250–73

Eslinger P W, Biegalski S R, Bowyer T W, Cooper M W, Haas D A, Hayes J C, et al. 2014 Source term estimation of radioxenon released from the Fukushima Dai-ichi nuclear reactors using measured air concentrations and atmospheric transport modeling *Journal of environmental radioactivity* **127** 127–132.

Fuka V and Brechler J 2012 Large eddy simulation modelling of the dispersion of radioactive particulate matter *Int. J. Environment and Pollution* **48** 156–63

Gallego E, Barbero R, Cuadra D, Domingo J and Iranzo A 2010 Modelling with a CFD code the near-range dispersion of particles unexpectedly released from a nuclear power plant *Proc. 3rd European IRPA Congress (Helsinki)* 14-8

Graham J 2012 *Fast Reactor Safety* (Elsevier) p 390

Hu Q-H, Weng J-Q and Wang J S 2010 Sources of anthropogenic radionuclides in the environment: a review *Journal of environmental radioactivity* **101** 426–37

IAEA 2002 Preparedness and response for a nuclear or radiological emergency *IAEA Safety Standards Series No. GS-R-2* (Vienna: International Atomic Energy Agency)

Kenis K, Vervecken L and Camps J 2013 Gamma dose assessment in near-range atmospheric dispersion simulations *External Report of the Belgian Nuclear Research Centre* ER-242

Nakayama H and Nagai H 2009 Development of Local-Scale High-Resolution Atmospheric Dispersion Model Using Large-Eddy Simulation Part 1: Turbulent Flow and Plume Dispersion over a Flat Terrain *Journal of Nuclear Science and Technology* **46** 1170–7

Nakayama H, Jurcakova K and Nagai H 2013 Development of local-scale high-resolution atmospheric dispersion model using large-eddy simulation. Part 3: turbulent flow and plume dispersion in building arrays *Journal of Nuclear Science and Technology* **50** 503–19

Önder A and Meyers J 2014 HPC realization of a controlled turbulent round jet using OpenFOAM *ArXiv e-prints* 1406.7231

Park W J, Han M H and Lee K J 2000 Analysis of the distributional effects of radioactive materials on external gamma exposure *Annals of Nuclear Energy* **27**(8), 659–71.

Punitha G, Sudha A J, Kasinathan N and Rajan M 2008 Atmospheric Dispersion of Sodium Aerosol due to a Sodium Leak in a Fast Breeder Reactor Complex *Journal of Power and Energy Systems* **2** 889–98

Raza S and Avila R 2001 A 3D Lagrangian particle model for direct plume gamma dose rate calculations *Radiological Protection* **21** 145–54

Rojas-Palma C, Aage H K, Astrup P, Bargholz K, IDrews M, Jørgensen H E, Korsbech U, Lauritzen B, Mikkelsen T and Thykier-Nielsen S 2004 Experimental evaluation of gamma fluence-rate predictions from Argon-41 releases to the atmosphere over a nuclear research reactor site *Radiation protection dosimetry* **108** 161–8

Slade D H 1968 *Meteorology and atomic energy* (Oak Ridge: US Atomic Energy Commission)

Trubey D K 1991 *New gamma-ray buildup factor data for point kernel calculations: ANS-6.4.3 standard reference data* (Washington, DC: Nuclear Regulatory Commission)

Vach M and Duong V M 2011 Numerical Modeling of Flow Fields and Dispersion of Passive Pollutants in the Vicinity of the Temelín Nuclear Power Plant *Environmental Modeling & Assessment* **16** 135–43

Wu P and Meyers J 2013 A constraint for the subgrid-scale stresses in the logarithmic region of high Reynolds number turbulent boundary layers: A solution to the log-layer mismatch problem *Physics of Fluids* **25** 015104

Xie D, Wang H and Kearfott K J 2012 Modeling and experimental validation of the dispersion of 222Rn released from a uranium mine ventilation shaft *Journal of Atmospheric Environment* **60** 453–9

Xie D, Wang H, Kearfott K J, Liu Z and Mo S 2014 Radon dispersion modeling and dose assessment for uranium mine ventilation shaft exhausts under neutral atmospheric stability *Journal of environmental radioactivity* **129** 57–62